



CHORUS

This is the accepted manuscript made available via CHORUS. The article has been published as:

Mapping domain-wall topology in the magnetic Weyl semimetal CeAlSi

Yue Sun, Changmin Lee, Hung-Yu Yang, Darius H. Torchinsky, Fazel Tafti, and Joseph Orenstein

Phys. Rev. B **104**, 235119 — Published 9 December 2021

DOI: [10.1103/PhysRevB.104.235119](https://doi.org/10.1103/PhysRevB.104.235119)

Mapping Domain Wall Topology in the Magnetic Weyl Semimetal CeAlSi

Yue Sun^{1,2,3}, Changmin Lee², Hung-Yu Yang⁴, Darius H. Torchinsky⁵, Fazel Tafti⁴, Joseph Orenstein^{1,2}

¹*Department of Physics, University of California, Berkeley, California 94720, USA*

²*Materials Science Division, Lawrence Berkeley National Laboratory, Berkeley, California 94720, USA*

³*Department of Chemistry, University of California, Berkeley, California 94720, USA*

⁴*Department of Physics, Boston College, Chestnut Hill, MA 02467, USA*

⁵*Department of Physics, Temple University, Philadelphia, Pennsylvania 19122, USA*

We report full vector mapping of local magnetization in CeAlSi, a Weyl semimetal in which both inversion and time-reversal symmetries are broken. The vector maps reveal unanticipated features both within domains and at their boundaries. Boundaries between domains form two kinds of walls with distinct topology and therefore different interactions with Weyl fermions. Domain walls aligned along the tetragonal axes, e.g. (100), exhibit emergent chirality forbidden by the bulk space group, while diagonal walls are non-chiral. Within the domains, we observe that the previously reported set of four easy axes aligned along the in-plane diagonals of the tetragonal structure actually split to form an octet with decreasing temperature below the magnetic transition. All the above phenomena are ultimately traced to the noncollinear magnetic structure of CeAlSi.

Weyl semimetals are condensed matter systems in which nondegenerate bands cross at isolated points, or nodes, in momentum space. Quasiparticles with momenta near the nodes are emergent Weyl fermions, exhibiting linear dispersion and definite chirality [1–3]. Although Weyl semimetals generally fall into inversion and time-reversal breaking classes, it is the magnetic, time-reversal breaking class that provides a means to generate and control emergent gauge fields with striking observable consequences [4–7].

CeAlSi is a hybrid of the two classes of Weyl semimetal introduced above, as its inversion-breaking (tetragonal) crystal structure generates Weyl nodes already in the paramagnetic state. Below the Curie temperature, T_c , of ≈ 8.5 K the local f -moments of Ce^{3+} order in a noncollinear ferromagnetic phase. The magnetization, which lies primarily in the ab plane, shifts the momenta of the nodes relative to their positions above T_c . Direct evidence for the dependence of nodal momenta on the magnetization direction was seen in the closely related compound CeAlGe, where domain wall resistance gives rise to highly singular structure in the anisotropic magnetoresistance [8]. Recent transport and scanning SQUID magnetometry measurements CeAlSi have reported novel anisotropic anomalous Hall effects [9] and the existence of magnetic domains with two distinct dynamic magnetic susceptibilities [10].

Gauge fields arise in magnetic Weyl semimetals (MWSMs) because the relative separation in momentum space of nodes of opposite chirality is governed by the local magnetization, which acts as an effective vector potential on the chiral charge [5, 11–13]. Consequently, considerable attention is focused on magnetic domain walls in MWSMs where temporal and spatial fluctuations of the magnetization are predicted to generate chiral electric and magnetic fields [14–19].

Here we report the topology of domain walls in CeAlSi, observed by mapping the magnetization vector field, $\mathbf{M}(\mathbf{r})$, using a scanning Kerr effect microscope. The magneto-optical Kerr effect (MOKE) is the rotation of

the plane of polarization on reflection from a medium with broken time-reversal symmetry [20]. At normal incidence, the MOKE signal, Θ , is sensitive only to the out-of-plane (z) component of the magnetization. However, upon changing the beam path to oblique incidence the polarization rotation becomes sensitive to the in-plane components of the magnetization as well [21–26]. When all three components of \mathbf{M} are present, Θ is a superposition of the polar, longitudinal, and transverse Kerr effects. For the measurements reported here, we developed a vector MOKE (VMOKE) method to disentangle these effects and obtain maps of all three components of the local magnetization vector.

VMOKE is based on measuring the dependence of Θ on the plane of linear polarization of the incident light. Figure 1(a) shows a schematic of the optical set-up. The incident polarization is controlled by a combination of a polarizer and a half-wave plate and Θ is measured with a balanced optical bridge detector (see Supplemental Material Section 1 [30]). Figure 1(b) shows a summary of the polarization dependence of Θ for the three Cartesian components of \mathbf{M} , where yz is the plane of incidence. In the usual convention, s and p polarization denote incident light polarization perpendicular and parallel to the plane of incidence, respectively. The polarization rotation resulting from M_z is independent of the incident polarization. M_y , which lies in the plane of incidence, generates a Kerr rotation that switches sign for s - and p -polarized input beams [23, 24]. Finally, M_x generates optical birefringence, leading to rotation on reflection that reverses sign when the incident polarization is rotated by $\pm 45^\circ$ with respect to the plane of incidence. Based on their distinct polarization dependences, we can determine the three components of \mathbf{M} at each location in the sample by performing three measurements: $\Theta(0)$, $\Theta(\pi/4)$, and $\Theta(\pi/2)$ (see Supplemental Material Section 2 [30]).

To eliminate long-term drifts and enhance sensitivity, we modulate Θ by overlapping the 780 nm probe beam with a 1560 nm pump beam chopped at 2.5 kHz. Lock-in detection at the chopping frequency allows for mea-

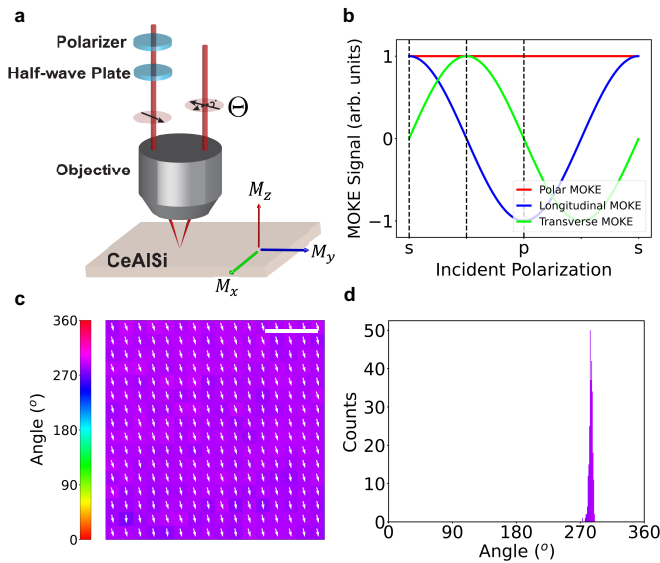


FIG. 1. (a) Schematic of the optical set-up of vector MOKE. The combination of a polarizer and a half-wave plate controls the incident polarization. The incident beam is focused by a 10x microscope objective. (b) Polarization dependence of polar, longitudinal and transverse contributions to the Kerr rotation, Θ . (c) Vector MOKE map of a single domain state in CeAlSi prepared by a 150 Oe magnetic field. The area of the region is $80 \mu\text{m} \times 80 \mu\text{m}$ and is sampled in $5 \mu\text{m}$ steps. Scale bar, $20 \mu\text{m}$. (d) Histogram of the magnetization direction in (c).

surement of Θ at the microradian level [27]. In order to validate our VMOKE measurement of the direction of the in-plane magnetization, we prepared a single domain state in CeAlSi by applying a 150 Oe magnetic field, which is stronger than the coercive field (70 Oe) [9]. The direction of the magnetic field (measured by a Hall effect magnetometer) was ≈ 10 from the [010] direction of the sample. The direction of the induced magnetization, as determined by scanning VMOKE, is shown by arrows in Figure 1(c); Figure 1(d) shows a histogram of the distribution of magnetization direction. The narrow narrow peak 280 matches the direction of the external magnetic field, confirming our method of determining the local in-plane magnetization direction. We have also carefully analyzed the second-order magneto-optical effect [28], which proves to be negligible in this case (see Supplemental Material Section 5 [30]).

Figure 2 presents spontaneous magnetization maps of CeAlSi at different temperatures. The sample was cooled under zero external magnetic field and the maps were measured during warming. The color code illustrates the direction of the in-plane magnetization \mathbf{M}_{\parallel} . The maximum out-of-plane component is approximately 1% of the in-plane components and will be discussed later. Clearly evident are large domains, of order $50 \mu\text{m}$ across, consistent with measurements performed at 6 K and above by scanning SQUID microscopy, which detects the near surface magnetic flux [10]. In the maps taken below 5

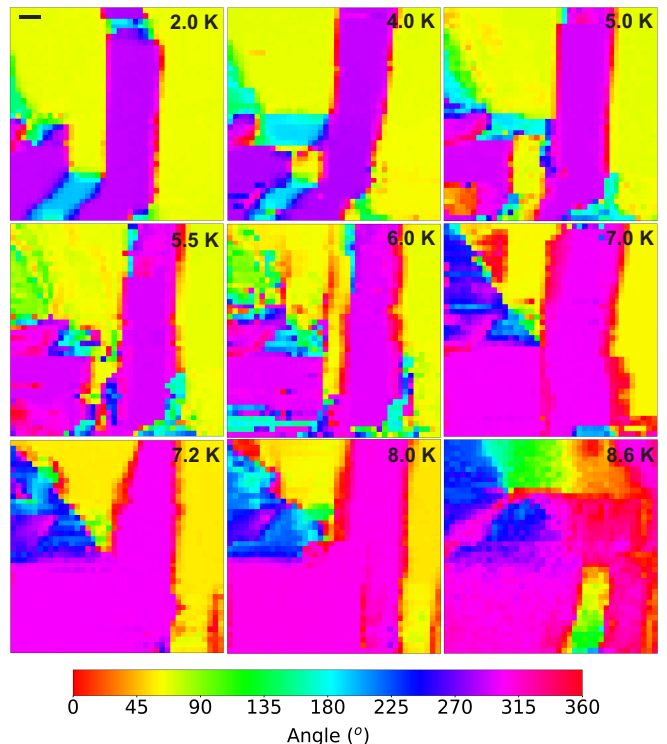


FIG. 2. Spontaneous magnetization map across a $200 \mu\text{m} \times 200 \mu\text{m}$ area of the sample from 2 to 8.6 K. Color code illustrates the direction of the in-plane magnetization. The color code is a color wheel, that is, 0 and 360 are indicated by the same color. Scale bar, $20 \mu\text{m}$.

K, both vertical and diagonal domain walls are observed. The domain structure changes with temperature variation as small as 0.5 K, and non-monotonically through the temperature range from 5-7 K, as on warming the domain pattern becomes first more disordered and then less disordered. The large fluctuations suggest that the domain walls are highly mobile at these intermediate temperatures. The map-average magnetization amplitude $|\mathbf{M}|$ goes to zero at ≈ 9 K (Figure 5(c)), which is close to the value of T_c (8.2 K) extracted from heat capacity measurement [9].

To organize the large information content of the maps of $\mathbf{M}(\mathbf{r})$, we consider first the orientation of \mathbf{M} within the domains. Previous studies of CeAlSi and the related compound CeAlGe concluded that the in-plane magnetization in zero field is oriented along four easy axis directions: (110) and the other three directions generated by the four-fold symmetry of the C_{4v} point group [8, 9]. However, the $\mathbf{M}(\mathbf{r})$ maps reveal that this is not the full story.

In Figure 3(a), we plot the distribution of magnetization directions at each of the measured temperatures. Two dominant angles are observed at every temperature, reflecting the fact that the maps are dominated by the purple and yellow domains. Some small cyan and green domains are also present in the maps. At temperatures

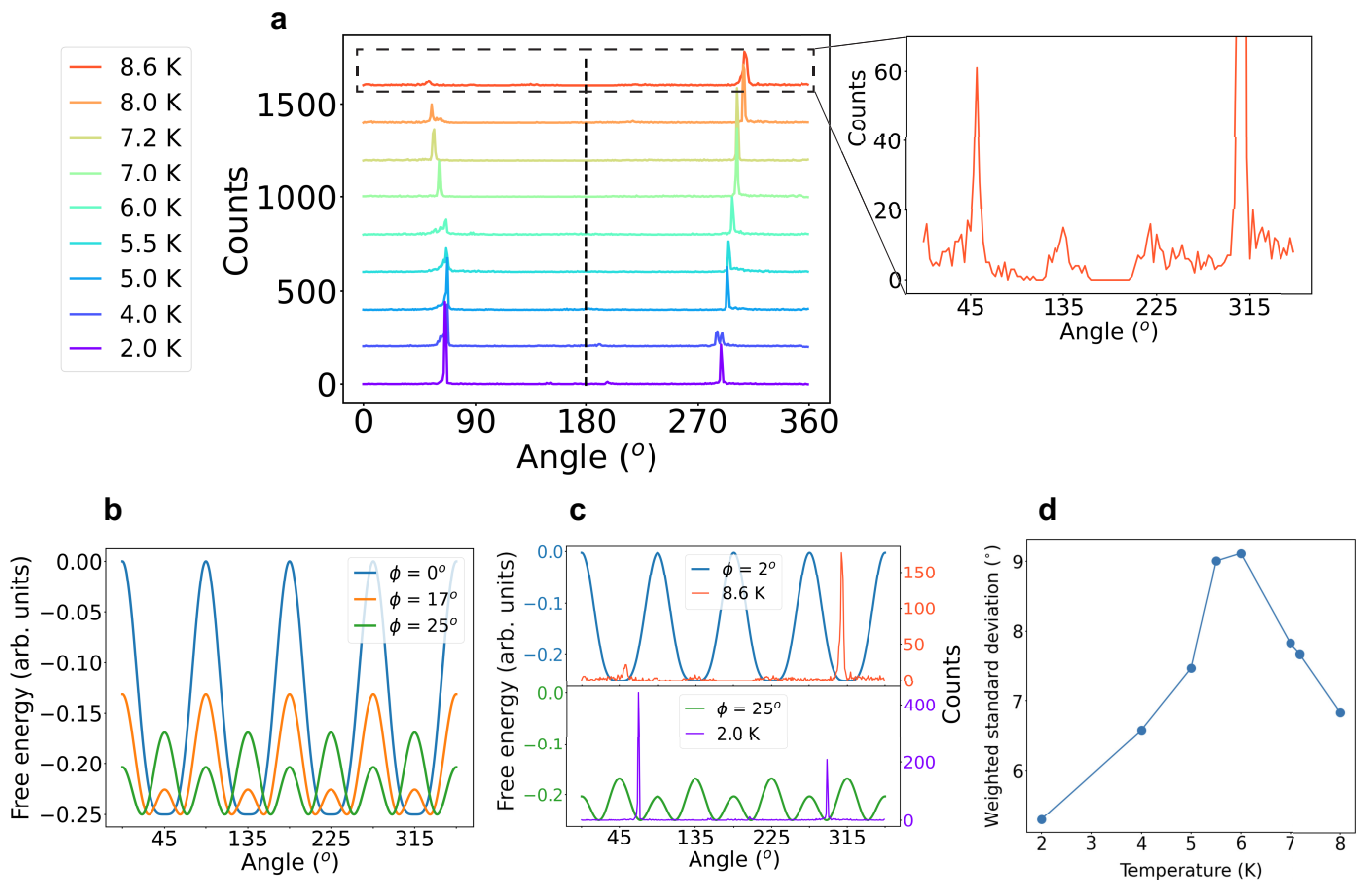


FIG. 3. (a) Histograms of the distribution of magnetization directions from 2 to 8.6 K. Expanded view, the histogram at 8.6 K. (b) Free energy as a function of θ with $\gamma = 1$, $\phi = 0, 17$ and 25 . (c) Comparison between the distribution of the magnetization direction and the free energy at 2 K and 8.6 K. (d) The weighted standard deviation of angle distribution in (a) as a function of temperature.

near T_c , the dominant angles are close to (110) and symmetry related directions, as can be seen in the expanded view of the 8.6 K data. However, it is clear that the peaks of the distribution begin to depart from these angles with cooling below about 5 K. At 2.0 K, the histogram peaks at 66 (yellow), 290 (purple), 200 (cyan) and 155 (green), have shifted from the previously reported easy axis directions by ≈ 25 . As this rotation of easy axes with decreasing temperature takes place, they remain symmetric with respect to 180, which is labeled as a dashed line in Figure 3(a).

To model rotation of the easy axes we construct a free energy based on the noncollinear magnetic order observed in neutron scattering measurements [9]. The CeAlSi structure is comprised of two alternating layers of Ce atoms, with magnetization \mathbf{M}_1 and \mathbf{M}_2 . The non-collinear order was shown to derive from an anisotropic g -tensor in isostructural CeAlGe [8]. Since the magnetization is mostly in-plane, we take only the x and y components into consideration. With the inclusion of interlayer coupling, the anisotropy energy F_a can be written in the form below, which respects the four-fold rotational

symmetry of the structure,

$$F_a = -\alpha (M_{1x}^2 M_{1y}^2 + M_{2x}^2 M_{2y}^2) + 4\beta M_{1x}^2 M_{1y}^2 M_{2x}^2 M_{2y}^2. \quad (1)$$

The first term is the anisotropy energy in each layer. Restricting the free energy to this term, which treats the two layers as independent, yields easy axes parallel to the [110] and symmetry related directions and therefore cannot account for the observed variation with temperature.

The second term is the interlayer coupling. Assuming ferromagnetic order in each layer, the directions of \mathbf{M}_1 and \mathbf{M}_2 can be expressed as $\theta + \phi$ and $\theta - \phi$, where θ is the direction of the net magnetization and 2ϕ is the angle spanned by \mathbf{M}_1 and \mathbf{M}_2 . Substituting the two angles into Equation (1), one finds

$$F_a \propto (1 - \gamma/2) \cos 4\phi \cos 4\theta + (\gamma/8)(\cos 8\theta + \cos 8\phi), \quad (2)$$

where $\gamma \equiv \beta/\alpha$. Figure 3(b) illustrates the free energy as a function of θ for $\gamma = 1$ and values of ϕ that are consistent with the neutron scattering measurements. For collinear magnetization ($\phi = 0$) the free energy minima occur at [110] and related directions. The four minima

split into eight with increasing ϕ ; note that the eight easy axes continue to respect the rotational and mirror symmetries of the crystal. All eight easy axes are observed in experiments (see Supplemental Material Section 9 [30]). Figure 3(c) compares the distribution of magnetization angles with the free energy at 2.0 K and 8.6 K, showing that temperature-dependent interlayer coupling captures the rotation of dominant angles observed in the Kerr maps. We note that the rotation of the easy axes can also be fit by allowing γ to vary with temperature with ϕ held constant (see Supplemental Material Section 8 [30]). The preference for a model in which ϕ varies is based on its correlation with the z component of the magnetization at domain boundaries, which is discussed later with reference to Figure 5.

As a bonus, the model may also account for the temperature dependence of the degree of disorder in the vector MOKE maps shown in Fig. 2. Qualitatively, it appears that the domain structure is more disordered at 6 K than at either higher or lower temperature. To quantify the degree of disorder we calculated the weighted average of the standard deviation of the angular distribution within each of the four peaks in Figure 3(a) (see Supplemental Material Section 10 for details [30]). The resulting weighted standard deviation, plotted in Figure 3(d), shows a clear maximum centered on 6 K. The maximum in disorder can be understood as a consequence of the flatness of the free energy minima that occurs at the transition from four to eight easy axes.

With this understanding of the magnetization within the domains, we next focus on the variations in $\mathbf{M}(\mathbf{r})$ that occur at the domain boundaries. Figure 4(a) is a map of M_z at 2 K, while Figure 4(b) shows the orientation of the in-plane magnetization measured at the same temperature using the same color scale as in Figure 1(a). The maps reveal vertically and diagonally oriented domain walls, i.e. parallel to [100] and [110], respectively, whose magnetization texture is topologically distinct. The contrasting texture can be seen in the expanded images shown in Figs. 4(c) and 4(d), in which arrows represent the local magnetization direction.

The contrasting character of the two walls is revealed by comparing the line cuts above and below the map in Figure 4(a). The upper line cut, which traverses two vertical domain walls, shows peaks in M_z whose sign depends on the sign of $\partial M_{para}/\partial n$, where M_{para} is the component of magnetization parallel to the wall and n is the normal coordinate. The cartoon in Figure 4(e) shows a side view of magnetization as the line cut traverses the two vertical domain walls (with the z component increased for clarity). The magnetization vector traces a highly eccentric ellipse when viewed from the plane of the map. The sense of the rotation is the same for the two boundaries, indicating that the domain walls are chiral. The same sense of chirality was observed for all vertical domains over multiple cool downs. In contrast, the line cuts through the diagonal domain walls depicted below Figure 4(a) show that in this case M_z goes continuously

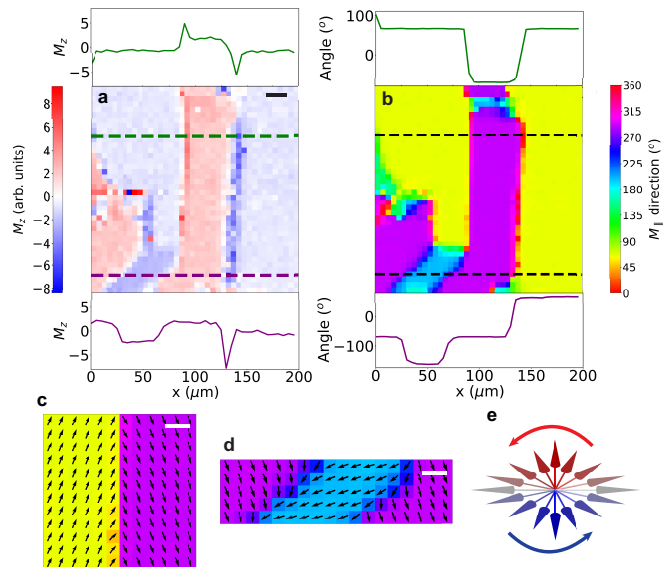


FIG. 4. (a) Map of the amplitude of M_z component at 2 K. The map is plotting the measured Kerr rotation as the unit of microradian, which is proportional to M_z . Scale bar, 20 μm . The line cuts above and below plot M_z along the lines with corresponding colors. (b) Spontaneous in-plane magnetization map at 2 K. The line cuts above and below plot the direction of in-plane magnetization along the same lines in (a). (c)(d) Expanded image of vertical and diagonal domain walls respectively. Arrows indicate the direction of in-plane magnetization. (e) Side view of magnetization as the line cut traverses the two vertical domain walls (with the z component increased for clarity).

through zero. We note that the walls differ as well in their magnetic charge density, $\sigma_M \equiv \mathbf{n} \cdot (\mathbf{M}_a - \mathbf{M}_b)$, which is of order M_{\parallel} in the diagonal walls and zero for the vertical walls, where \mathbf{M}_a and \mathbf{M}_b denote the magnetization on both sides of the domain wall. Thus chiral magnetic charge neutral and non-chiral charged domain walls coexist in CeAlSi.

The observation of chirality is surprising as the required Lifshitz invariant, $DM_z(\nabla \times \mathbf{M})_z$, is forbidden in the bulk of the crystal by the mirror symmetry that takes $x \rightarrow -x$ [29]. However, the noncollinear ordering of the magnetic bilayers within the unit cell can break the mirror symmetry at the domain boundary, permitting $DM_z(\nabla \times \mathbf{M})_z \neq 0$ (see Supplemental Material Section 6 [30]). Figure 5(a), which is a map of $(\nabla \times \mathbf{M})_z$, shows that the difference in chirality of the two types of walls is consistent with the picture of a local gyromagnetic invariant. As seen in the line cut through the vertical walls, $(\nabla \times \mathbf{M})_z$ peaks at the domain boundaries, reproducing the structure in M_z shown previously, while the line cut through the diagonal domain wall shows that $(\nabla \times \mathbf{M})_z = 0$ at the nonchiral boundary.

We have argued above that the existence of a local chirality-generating term in the free energy is a consequence of the noncollinear magnetic ordering. Further support for this hypothesis is seen in Figure 5(b),

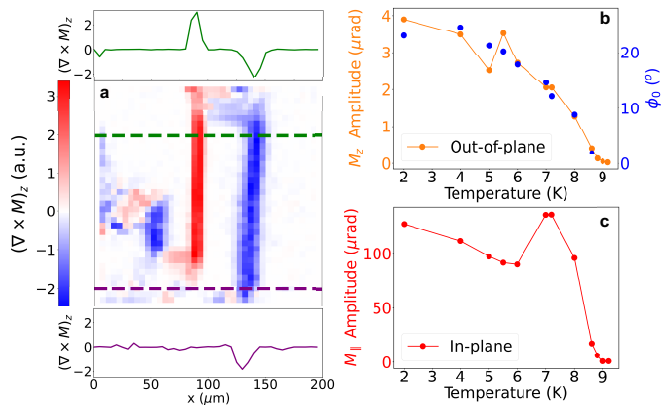


FIG. 5. (a) Map of $(\nabla \times \mathbf{M})_z$ at 2 K. Scale bar, $20 \mu\text{m}$. The line cuts above and below plots $(\nabla \times \mathbf{M})_z$ along the lines with corresponding colors. (b) The amplitude of M_z and ϕ as a function of temperature. Orange dots: M_z amplitude in chiral domain boundaries. Blue dots: ϕ extracted by fitting the histogram in each temperature. (c) The map-averaged amplitude of $M_{||}$ as a function of temperature. We attribute the dip in amplitude at 6 K to the disordering of the domain patterns that occurs in temperature range from 5-7 K.

which compares the temperature dependence of the wall-centered peak in M_z with ϕ , the angle between the magnetization in adjacent layers as deduced from the shift of the in-plane easy axes. The proportionality of these observables supports a causal relation between in-plane noncolinearity and domain wall chirality. Both quantities onset more gradually with decreasing temperature than the magnetization itself, whose T dependence is shown in Figure 5(c).

In summary, we have reported full vector imaging of magnetization in the magnetic Weyl semimetal CeAlSi, revealing new properties causally connected to its non-collinear magnetic structure. Coupling between adjacent noncollinear layers of Ce moments splits the conventional four-fold pattern of in-plane easy axes to an octet and leads to the formation of two classes of domain walls. The walls exhibit contrasting behavior in both chirality and local magnetic charge density. In the charge-neutral walls aligned along the in-plane tetragonal crystal axes, the magnetization traces an elliptical orbit as the wall is traversed, while the charged walls that form parallel to (110) are nonchiral. The existence of walls with distinct topology will enable future tests of the role of magnetic texture in determining emergent gauge fields in Weyl magnets and their coupling to real external fields. Strong hints of distinct responses to external fields corresponding to the two classes of domains walls have already been seen in local measurements of ac susceptibility [10] and serve as additional motivation for future studies.

ACKNOWLEDGMENTS

Optical measurements and analysis were performed at the Lawrence Berkeley Laboratory as part of the Quantum Materials program, Director, Office of Science, Office of Basic Energy Sciences, Materials Sciences and Engineering Division, of the U.S. Department of Energy under Contract No. DE-AC02-05CH11231. J.O and Y.S received support from the Moore Foundation's EPIQS Initiative through Grant GBMF4537 to J.O. at UC Berkeley. The work at Boston College was funded by the National Science Foundation under award No. DMR-1708929.

-
- [1] A. Bansil, H. Lin, and T. Das, *Rev. Mod. Phys.* **88**, 021004 (2016).
- [2] N. Armitage, E. Mele, and A. Vishwanath, *Rev. Mod. Phys.* **90**, 015001 (2018).
- [3] X. Wan, A. M. Turner, A. Vishwanath, and S. Y. Savrasov, *Phys. Rev. B* **83**, 205101 (2011).
- [4] N. Nagaosa, T. Morimoto, and Y. Tokura, *Nat Rev Mater* **5**, 621 (2020).
- [5] R. Ilan, A. G. Grushin, and D. I. Pikulin, *Nat Rev Phys* **2**, 29 (2020).
- [6] D. Destraz, L. Das, S. S. Tsirkin, Y. Xu, T. Neupert, J. Chang, A. Schilling, A. G. Grushin, J. Kohlbrecher, L. Keller, P. Puphal, E. Pomjakushina, and J. S. White, *npj Quantum Mater.* **5**, 5 (2020).
- [7] X. Yuan, C. Zhang, Y. Zhang, Z. Yan, T. Lyu, M. Zhang, Z. Li, C. Song, M. Zhao, P. Leng, M. Ozerov, X. Chen, N. Wang, Y. Shi, H. Yan, and F. Xiu, *Nat Commun* **11**, 1259 (2020).
- [8] T. Suzuki, L. Savary, J.-P. Liu, J. W. Lynn, L. Balents, and J. G. Checkelsky, *Science* **365**, 377 (2019).
- [9] H.-Y. Yang, B. Singh, J. Gaudet, B. Lu, C.-Y. Huang, W.-C. Chiu, S.-M. Huang, B. Wang, F. Bahrami, B. Xu, J. Franklin, I. Sochnikov, D. E. Graf, G. Xu, Y. Zhao, C. M. Hoffman, H. Lin, D. H. Torchinsky, C. L. Broholm, A. Bansil, and F. Tafti, *Phys. Rev. B* **103**, 115143 (2021).
- [10] B. Xu, J. Franklin, A. Jayacody, H.-Y. Yang, F. Tafti, and I. Sochnikov, *Advanced Quantum Technologies* <https://doi.org/10.1002/qute.202000101> (2021).
- [11] C.-X. Liu, P. Ye, and X.-L. Qi, *Phys. Rev. B* **87**, 235306 (2013).
- [12] H. Shapourian, T. L. Hughes, and S. Ryu, *Phys. Rev. B* **92**, 165131 (2015).
- [13] A. Cortijo, Y. Ferreirs, K. Landsteiner, and M. A. Vozmediano, *Phys. Rev. Lett.* **115**, 177202 (2015).
- [14] Y. Araki, *Annalen der Physik* **532**, 1900287 (2020).
- [15] J. D. Hannukainen, Y. Ferreiros, A. Cortijo, and J. H. Bardarson, *Phys. Rev. B* **102**, 241401 (2020).
- [16] A. A. Zyuzin and V. A. Zyuzin, *Phys. Rev. B*, 4 (2015).
- [17] F. R. Lux, F. Freimuth, S. Blgel, and Y. Mokrousov, *Commun Phys* **1**, 60 (2018).
- [18] S. Tchoumakov, M. Civelli, and M. O. Goerbig, *Phys. Rev. B* **95**, 125306 (2017).
- [19] L. Liang and T. Ojanen, *Phys. Rev. Research* **2**, 022016 (2020).
- [20] J. McCord, *J. Phys. D: Appl. Phys.* **48**, 333001 (2015).
- [21] Z. Q. Qiu and S. D. Bader, *Review of Scientific Instru-*

- ments **71**, 1243 (2000).
- [22] A. Stupakiewicz, A. Chizhik, M. Tekielak, A. Zhukov, J. Gonzalez, and A. Maziewski, *Review of Scientific Instruments* **85**, 103702 (2014).
- [23] W. Rave, R. Schfer, and A. Hubert, *Journal of Magnetism and Magnetic Materials* **65**, 7 (1987).
- [24] Z. J. Yang and M. R. Scheinfein, *Journal of Applied Physics* **74**, 6810 (1993).
- [25] C. Daboo, J. A. C. Bland, R. J. Hicken, A. J. R. Ives, M. J. Baird, and M. J. Walker, *Phys. Rev. B* **47**, 11852 (1993).
- [26] H. Ding, S. Ptter, H. Oepen, and J. Kirschner, *Journal of Magnetism and Magnetic Materials* **212**, 5 (2000).
- [27] A. Little, C. Lee, C. John, S. Doyle, E. Maniv, N. L. Nair, W. Chen, D. Rees, J. W. F. Venderbos, R. M. Fernandes, J. G. Analytis, and J. Orenstein, *Nat. Mater.* **19**, 1062 (2020).
- [28] R. M. Osgood, B. M. Clemens, and R. L. White, *Phys. Rev. B* **55**, 8990 (1997).
- [29] A. Ullah, B. Balamurugan, W. Zhang, S. Valloppilly, X.-Z. Li, R. Pahari, L.-P. Yue, A. Sokolov, D. J. Sellmyer, and R. Skomski, *IEEE Trans. Magn.* **55**, 1 (2019) .
- [30] See Supplemental Material at [URL will be inserted by publisher] for details of experimental set-up and balanced optical bridge detector, details of macroscopic vector MOKE model, second-order magneto-optical effect, observation of eight domain variants, clarification of the free energy model, statistics of global disorder and local mirror symmetry breaking.